



# Dependence of microstructures on fatigue performance of polycrystals: A comparative study of conventional and additively manufactured 316L stainless steel

Luqing Cui<sup>a</sup>, Fuqing Jiang<sup>b</sup>, Ru Lin Peng<sup>a</sup>, Reza Taherzadeh Mousavian<sup>c</sup>,  
Zhiqing Yang<sup>b,d,\*</sup>, Johan Moverare<sup>a,\*</sup>

<sup>a</sup> Division of Engineering Materials, Department of Management and Engineering, Linköping University, Linköping SE-58183, Sweden

<sup>b</sup> Shenyang National Laboratory for Materials Science, Institute of Metal Research, Chinese Academy of Sciences, Shenyang 110016, China

<sup>c</sup> I-Form, Advanced Manufacturing Research Centre, Dublin City University, Dublin 9, Ireland

<sup>d</sup> Ji Hua Laboratory, Foshan 528200, China

## ARTICLE INFO

### Keywords:

Fatigue behavior

316 L

Additive manufacturing

Unique microstructure characteristics

Deformation mechanisms

## ABSTRACT

The fatigue properties and microstructural evolution of 316 L stainless steel (316LSS) manufactured by laser powder bed fusion (L-PBF) were systematically studied and compared with its wrought counterpart. The as-built L-PBF 316LSS shows a pronounced heterogeneity, not only structurally but also chemically, with a unique microstructure of highly serrated grain boundaries, bimodal grain structure, nano-precipitates, solidification cell structures, and chemical segregations. The microindentation test showed that the hardness of the as-built L-PBF 316LSS reached 2.589 GPa, which was about 1.6 times higher than that of the wrought solution annealed counterpart, and the sparser slip steps around indentations revealed its greater dislocation storage capability. The S-N curves indicated that the fatigue resistance of the as-built L-PBF 316LSS was significantly better than that of the wrought solution annealed samples, and this was ascribed to its unique microstructural characteristics, especially the pre-existing high-density dislocations and chemical microsegregation within cellular solidification features. Furthermore, the enhanced planar slip in L-PBF 316LSS by its unique microstructure, especially the formation of deformation twins, delays the strain localization and restrains slip band generation, thereby significantly inhibiting crack initiation, and contributing greatly to the fatigue performance. The unique cell structure appears to be more effective in improving the low-cycle fatigue performance of L-PBF 316LSS due to the enhanced ductility.

## 1. Introduction

As one of the most promising technologies in the field of metal additive manufacturing (AM), laser powder bed fusion (L-PBF) also known as selective laser melting (SLM) has attracted huge attention (Deng et al., 2021; Liu et al., 2018). The ultrafast cooling rate and significant solute partition during the L-PBF process lead to the distinctly different as-built microstructure compared to material fabricated by conventional approaches (Deng et al., 2021; Li et al., 2020b). For polycrystalline metallic materials, such as austenitic

\* Corresponding authors.

E-mail addresses: [yangzq@imr.ac.cn](mailto:yangzq@imr.ac.cn) (Z. Yang), [johan.moverare@liu.se](mailto:johan.moverare@liu.se) (J. Moverare).

<https://doi.org/10.1016/j.ijplas.2021.103172>

Received 6 November 2021; Received in revised form 2 December 2021;

Available online 5 December 2021

0749-6419/© 2021 The Author(s). Published by Elsevier Ltd. This is an open access article under the CC BY license

(<http://creativecommons.org/licenses/by/4.0/>).

stainless steels (Cui et al., 2021a) and high entropy alloys (Kim et al., 2022), the L-PBF components usually exhibit an overwhelming advantage in terms of mechanical properties over the structures manufactured by other traditional processes (Liu et al., 2018; Nakada et al., 2010; Wang et al., 2018). The investigations related to austenitic stainless steels (SS), such as 316LSS (Bronkhorst et al., 2019; Li et al., 2020b), 308LSS (Li et al., 2020a) and 304LSS (Pokharel et al., 2019), have been extensively carried out from the academia to manufacturing industries (AlMangour et al., 2019). However, most of them were focused on the relationship between process parameter optimization, microstructure adjustment and monotonic mechanical properties. The reliability and deformation mechanism of these L-PBF austenitic stainless steels under cyclic loading conditions still require in-depth research. Some intrinsic defects, such as lack-of-fusion (LOF) (Darvish et al., 2016), surface roughness (Kahlin et al., 2020; Yu et al., 2020), keyhole collapse (Cunningham et al., 2019) and gas porosity (Svensson et al., 2010) etc., can be introduced during the L-PBF process, which notably affect the fatigue properties of AM parts. Compared with the irregular shape defects, it was reported that the small spherical defects had less effect on the initiation of fatigue cracks (Smith et al., 2019b). The influence of internal defects and residual stress on the fatigue resistance of L-PBF 304LSS were also compared, and results showed that the former had a more remarkable impact (Zhang et al., 2020). Furthermore, the surface defects could bring about a more significant reduction in fatigue life for L-PBF 316LSS, since the fatigue cracks usually tend to initiate from the surface (Andreau et al., 2021; Maleki et al., 2021). Additionally, some measures also have been employed to tailor the microstructures of L-PBF alloys to enhance their fatigue resistance. The study by Elangeswaran et al. (Elangeswaran et al., 2020) revealed that the as-built L-PBF 316LSS exhibited a fatigue strength of 50 MPa higher than its annealed counterparts under the fatigue life of  $10^5$  cycles. Similar results were also reported by other researchers (Cao et al., 2020; Pegues et al., 2020). Therefore, the excellent fatigue performance of AM alloys appears to have a close relationship with their unique microstructure features produced during the manufacturing process. Nevertheless, to the best of the authors' knowledge, the effect of unique microstructure characteristics on the fatigue properties of AM alloys is still poorly understood.

Motivated by the above considerations, the mechanism of unique microstructure features on the fatigue resistance of AM 316LSS was systematically studied with the help of multidisciplinary characterization techniques. The AM 316LSS was manufactured by L-PBF with optimized process parameters, and the obtained components were near fully dense with a relative density higher than 99.9%. To minimize the effect of surface scratches, all samples were mechanically polished to a surface roughness of  $0.2 \mu\text{m}$ . Furthermore, comparisons were also conducted with the conventionally manufactured counterpart. Results showed that the fatigue resistance of the as-built L-PBF 316LSS was much higher compared with wrought and solution annealed 316LSS. The unique microstructural characteristics (i.e., the pre-existing high-density dislocations, bimodal grain structure, cell structures and chemical segregations), together with the planar dislocation substructures induced during cyclic loading were considered to be responsible for the greater fatigue resistance of L-PBF 316LSS.

## 2. Materials and method

### 2.1. Material preparation

For details of the 316LSS powder used in this work, please refer to our previous work (Cui et al., 2022a, 2021a). EOSINT M280 3D machine was adopted to vertically manufacture the cylindrical bars with a length of 60 mm and a diameter of 10 mm (Fig. 1b) under high-purity argon. To minimize defects (such as voids, balling, lack of fusion, etc.), the process parameters had been optimized, with a laser power of 195 W, a hatch space of  $90 \mu\text{m}$ , a laser scanning speed of 1083 mm/s, a layer thickness of  $20 \mu\text{m}$  and a spot size of  $75 \mu\text{m}$ . A bidirectional scanning strategy was employed during the entire L-PBF process, and after one layer is complete the scanning direction will rotate  $67^\circ$  for the subsequent layer, as illustrated in Fig. 1a. The  $67^\circ$  laser rotation gives the maximum number of layers until the same scan vector appears again (Pakkanen, 2018), resulting in relatively isotropic mechanical properties and microstructural refinement. The combined parameter describing the volume energy density (VED) is an important factor for the manufacturability of AM alloys and is sensitive to the porosity of the microstructure (Cherry et al., 2015). As reported in Ref. (Cherry et al., 2015; Nayak

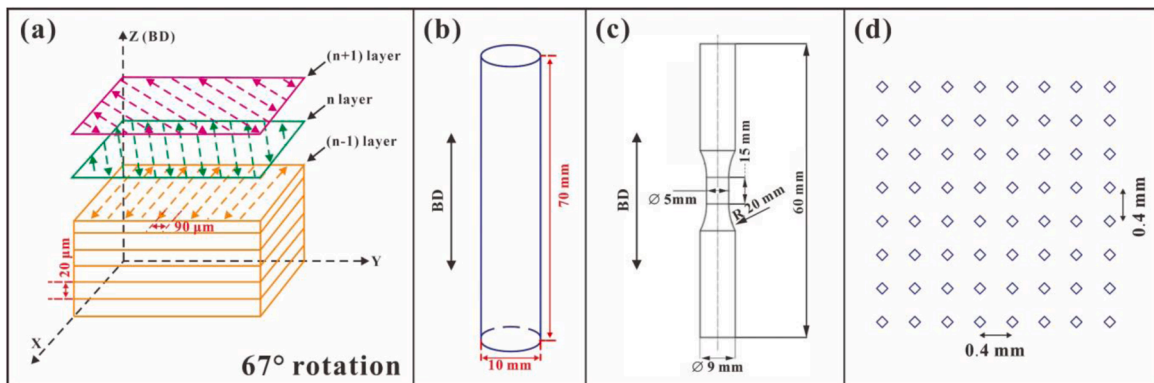


**Fig. 1.** 3D-illustration of the scanning strategy applied in the present work. The rotation angle of the scanning direction between adjacent layers is  $67^\circ$ . (b)-(c) Geometries of the as-manufactured cylinders and fatigue samples, respectively. (d) Schematic illustration of the microindentation test.

et al., 2020), the appropriate VED value for 316LSS to obtain near-zero porosity microstructure was around  $100 \text{ J/mm}^3$ , and can be calculated as follows:

$$\text{VED} = \frac{P}{vht} \quad (1)$$

where  $P$ ,  $v$ ,  $h$ ,  $t$  are laser power, laser scan speed, hatch space and layer thickness respectively. Therefore, the VED for the present case is determined to be  $100 \text{ J/mm}^3$ , which is in good agreement with the previously reported data (Cherry et al., 2015; Nayak et al., 2020), and also implies that the L-PBF 316LSS used in this study might have very low porosity. For comparison, conventional 316LSS were also studied in the fully annealed condition ( $1060^\circ\text{C}$  for 40 min) of cold-rolled bars. To distinguish from the L-PBF ones, the conventional counterparts were named as W316LSS in the following text.

### 2.3. Microindentation hardness and stress control fatigue testing

Microindentation tests were carried out on a LECO hardness machine both for L-PBF and wrought 316LSS using a maximum load of 2.45 N and a dwell-time of 15 s. The distribution of indentations with an adjacent distance of 0.4 mm were schematically shown in Fig. 1d, and the hardness was the average value of more than 60 indentations. Furthermore, to reveal the blocking effect of the unique microstructural characteristics (i.e., highly serrated grain boundaries (GBs), cell structures and, melt pool boundaries) in AM alloys on the dislocation motion, the slip traces around indentations of the same orientation grains in L-PBF and wrought 316LSS were studied in detail.

Fatigue samples with the geometry illustrated in Fig. 1c were machined from the L-PBF and wrought 316LSS bars. Before the fatigue deformation, all samples were mechanically polished to a surface roughness of  $R_z = 0.2 \mu\text{m}$  to minimize the effect of surface scratches and other surface features such as semi-melted, unmelted powders and fusion line defects. Stress-controlled fatigue tests were performed on a servo-hydraulic fatigue rig with a frequency of 5 Hz and a stress ratio of  $R = -1$  at room temperature. The applied stress was adjusted after each test to cover the fatigue life of  $10^4$  to  $10^6$  with the few fatigue samples available. More information about fatigue testing can be found in our previous work (Cui et al., 2022a, 2021a).

#### 2.4. Microstructural characterizations

Multiple probing methods were employed to characterize the microstructural evolution of the two samples prior to and after deformation. Electron backscattered diffraction (EBSD) analysis was performed on a Hitachi SU70 FEG scanning electron microscope (SEM) equipped with a Nordlys-S™ detector. For SEM and EBSD, thin strips parallel to the loading direction were cut from the gage section of samples by electro-discharge machining. Then these strips were ground utilizing abrasive papers (#500–4000 grit), and

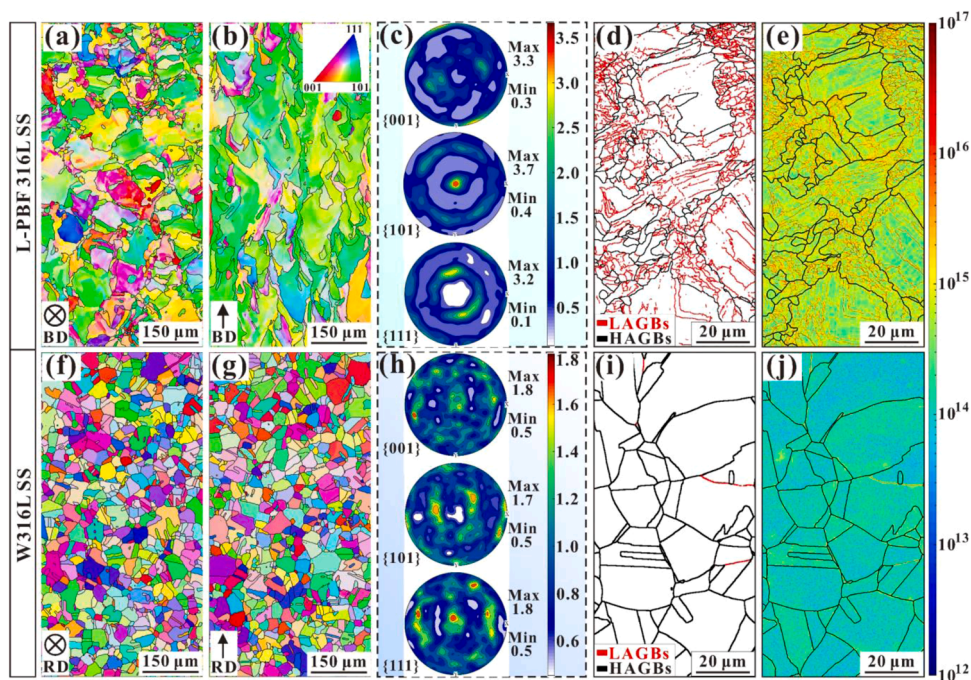


**Fig. 2.** EBSD IPF maps and corresponding PF of the L-PBF (a-c) and wrought (f-h) 316LSS. EBSD grain boundary and corresponding GND density distribution maps of the L-PBF (d-e) and wrought (i-j) 316LSS.

further polished using a silica colloidal suspension. The working distance, tilt angle and accelerating voltage for EBSD were set to 27 mm, 70° and 20 kV, respectively. To accurately determine the density of geometrically necessary dislocations (GNDs), an appropriate step size of 200 nm was selected during the EBSD scan, which is small enough to reveal the dislocation substructures in the present L-PBF 316LSS and large enough to provide an acceptable measurement duration. The acquired EBSD data were processed by HKL Channel 5 software and MATLAB MTEX toolbox (Cui et al., 2021b). The calculation of GND density was based on the Pantleon's theory (Pantleon, 2008), which has been extensively applied to many polycrystalline alloys, such as Mg alloy AZ31 (Paramatmuni and Dunne, 2020), high purity tungsten single crystal (Das et al., 2018), commercial purity titanium (Zhu et al., 2017) and nickel-based superalloys (Biroasca et al., 2019; Witzten et al., 2020). Moreover, the misorientation of 15° was applied to separate the high angle GBs (HAGBs) from the low angle GBs (LAGBs), and 5  $\mu\text{m}$  was set as the minimum grain size. The deformation mechanisms during deformation and the characteristic cell structures in L-PBF 316LSS were analyzed using FEI Tecnai G2 and the aberration-corrected Titan 60–300 TEM. The energy dispersive X-ray spectrometers (EDS) equipped in SEM and TEM were also employed to detect the chemical compositions of cellular structures and precipitates. All TEM samples were prepared using a twin-jet electro-polisher and a solution of 10 vol% perchloric acid and 90 vol% ethanol at 25 V and  $-25^\circ\text{C}$ .

### 3. Results

#### 3.1. Grain structure

Figs. 2a-2e and 2f-2j show the EBSD-acquired inverse pole figure (IPF), corresponding pole figures (PF), GB and GND density distribution maps of L-PBF and wrought 316LSS, respectively. The IPF maps in Figs. 2a-2b confirm that the L-PBF 316LSS possesses a heterogeneous grain structure. The plane perpendicular to BD contains equiaxed grains and banded grain structure with a width of about 85  $\mu\text{m}$  (Fig. 2a), which agrees well with the adopted laser hatch space (Fig. 1a). Nevertheless, columnar grains with highly serrated GBs were present on the plane parallel to BD (Fig. 2b). The significantly different microstructures on the two perpendicular planes are due to the larger hatch space (90  $\mu\text{m}$ ) compared to the layer thickness (20  $\mu\text{m}$ ) leading to the epitaxial growth of grains. In other words, the melt pools partially overlap and re-melt during the L-PBF process, which is necessary for the deposited powder to fully melt. Distribution of grain sizes in Figs. 2a and 2b are also measured, as one example illustrated in Fig. 3a1, and the average values are  $16.66 \pm 14.59$  and  $21.02 \pm 22.45$   $\mu\text{m}$ , respectively. The reason for the large standard deviation is the high fraction of small-sized  $\langle 001 \rangle$  orientated grains separated by the low content of large-sized  $\langle 101 \rangle$  ones, as shown in Figs. 2a-2b and Fig. 3a. For face-centered cubic (FCC) crystals, the  $\langle 001 \rangle$  texture is dominant in L-PBF alloys, because it is easier to grow along the temperature gradient (Cui et al., 2022b). However, in our case highly developed  $\langle 101 \rangle$  texture was generated with BD as the reference axis. In this regard, the maximum of multiples of uniform density (mud), as illustrated in Fig. 2c, was measured as 3.3, 3.7, and 3.2 for  $\{001\}$ ,  $\{101\}$  and  $\{111\}$  grains, respectively. By performing neutron diffraction analysis, the study by Yu et al. (Yu et al., 2020) demonstrated a clear fiber texture transition from  $\langle 101 \rangle$  to  $\langle 001 \rangle$  as the samples became thinner. By tuning the scanning strategy, a strong  $\langle 001 \rangle$  texture was

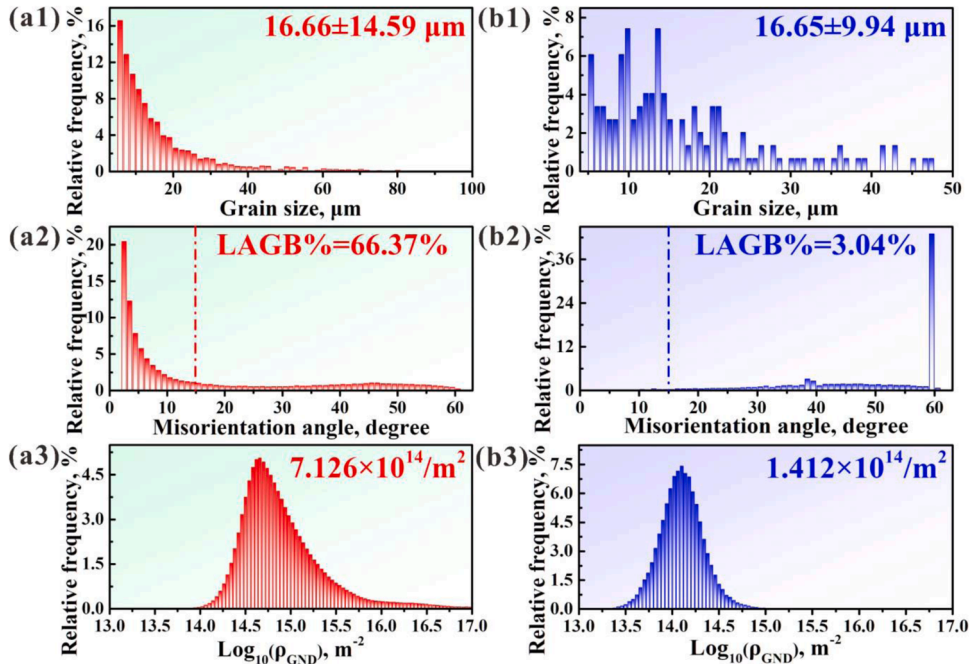


**Fig. 3.** Distribution of grain size, grain boundary misorientation and GND density in logarithmic scale for the L-PBF (a) and wrought (b) 316LSS, respectively.



also formed in the L-PBF Ni-25 at.%Mo alloys (Sun et al., 2018a). Similarly, Sun et al. (Sun et al., 2018b) reported that fine-grained  $\langle 101 \rangle$  texture was introduced while  $\langle 001 \rangle$  texture was weakened as the scanning strategy was varied for L-PBF 316LSS. As a consequence, the formation of  $\langle 101 \rangle$  texture in the present work might be greatly affected by the sample thickness and scanning strategy.

Contrarily, as shown in Figs. 2f-2h, distinctly different grain structures and orientations were present in the W316LSS. Both planes perpendicular and parallel to the rolling direction (RD) were composed of equiaxed grains with an average size of  $16.65 \pm 9.94 \mu\text{m}$  (Figs. 2f, 2g and 3b1), and more spread textures were formed (Fig. 2h) in the W316LSS. Additionally, the GND densities of the two samples were measured using the Hough-based EBSD method (Cui et al., 2021b). From Figs. 2d and 2e, it can be seen that GNDs were heterogeneously distributed in the microstructure, most of which were concentrated along LAGBs. The GND density of the L-PBF 316LSS was calculated to be about  $7.126 \times 10^{14}/\text{m}^2$  (Fig. 3a3), which is almost 5 times of the wrought sample (Fig. 3b3). This indicates that a high density of dislocations is introduced during the solidification of the L-PBF process, which is attributed to strong mechanical constraints from the substrate and the ultrafast cooling rate (Smith et al., 2019a). During the AM process, approximately 2% thermal strain is generated in the AM-manufactured materials, hence numerous dislocations are required to compensate for this difference (Kim et al., 2021). This is also verified by the high concentration of LAGBs in the L-PBF 316LSS (66.37% in length in Fig. 3a2), namely the generated GNDs during the manufacturing process transform themselves into the energetically favorable configurations (LAGBs) to compensate the thermal strain. As a comparison, the cold-working induced strain has been completely eliminated by the high-temperature annealing, as indicated by the low GND density in Figs. 2j and 3b3.

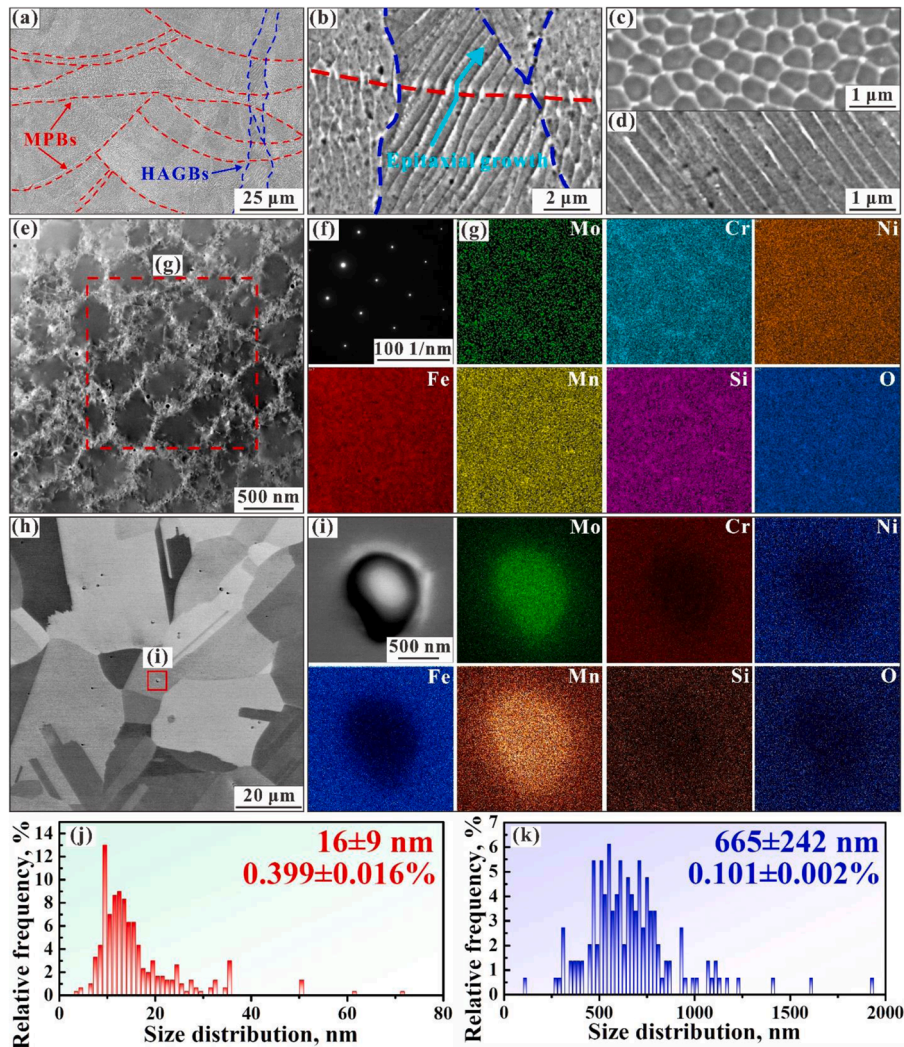


**Fig. 4.** (a)-(d) Cross-sectional SEM micrographs revealing MPBs, HAGBs, epitaxial growth of grains and solidification cellular structures. (e)-(g) A HAADF STEM micrograph and corresponding EDS maps showing the segregation of chemical compositions in the cell structures. (f) Selected area electron diffraction (SAED) pattern of Fig. 4e. (h)-(i) A SEM micrograph and corresponding EDS maps illustrating segregation of Mo and Mn to the precipitates. (j) and (k) The size distributions of the precipitates in L-PBF and wrought 316LSS, respectively.

### 3.2. Cell structures and precipitates

SEM micrographs in Figs. 4a–4d together with the high-angle annular dark-field (HAADF) micrograph in Fig. 4e and its corresponding STEM-EDS maps in Fig. 4g reveal the heterogeneity of the L-PBF 316LSS, not only structurally but also chemically, with semi-elliptical melt pool boundaries (MPBs), highly serrated GBs, epitaxial growth of grains, nano-precipitates, solidification cell structures, and chemical segregations. Twins are not present in the microstructure. Of particular interest are the cell structures, consisting of tangled dislocations on the walls and sparse dislocations inside (see the HAADF image in Fig. 4e), which can be frequently observed in L-PBF alloys (Liu et al., 2018; Wang et al., 2018). According to the viewing direction, various appearances of cellular structures can be obtained, such as the equiaxed and columnar morphologies in Figs. 4c and 4d. A modified Hall–Petch theory related to cell structures, namely treating the cell walls as HAGBs, were widely adopted to rationalize the high yield strength of AM alloys, and their calculation was in good conformity with the experimental result (Wang et al., 2018). Besides, the in-situ tensile test with the help of TEM revealed that the motion of activated dislocations could be slow down by the cell walls (Liu et al., 2018). Although the strengthening mechanism of cell structures is different from HAGBs due to their low misorientation (below than  $2^\circ$  (Wang et al., 2018)), it still can prove that the pre-existing cell structures play a significant contributor to the 308 MPa increase in the yield strength of L-PBF 316LSS compared to its conventional counterpart (Liu et al., 2018). On the other hand, our STEM-EDS mapping of the present L-PBF 316LSS illustrates the segregation of Cr and Mo along the cell walls (Fig. 4f). This means that the cell structures in our work are not only formed by dislocation networks, but also by chemical microsegregation, which makes them different from the cellular dislocation substructures in deformed conventional alloys (Nabil Bassim and Klassen, 1986), even though they have morphological similarities.

From the selected area electron diffraction (SAED) pattern in Fig. 4f, only the austenite matrix with FCC structure can be detected without the characterization of nano-precipitates on the cell walls (Fig. 4e). Nevertheless, based on the STEM-EDS mapping in Fig. 4j, Si- and O-enriched secondary phase particles were indeed in-situ formed on the cell walls during the manufacturing process. The presence of nano-precipitates has been discovered in many metallic materials fabricated by additive manufacturing (Salman et al., 2019; Wang et al., 2018; Yan et al., 2018). Yan et al. (2018) reported that the normally detrimental inclusions in conventional counterparts could be transformed into beneficial nano-particles in L-PBF 316LSS. These precipitates serve as Zener-pinning points and offer dragging force during heat treatments to prevent grain growth, thereby strengthening the material (Yan et al., 2018). Salman et al. (2019) and Wang et al. (2019) also confirmed the generation of nano-scale oxide particles on the cell walls after the L-PBF process. It is well known that dispersion strengthening is governed by the interaction of Orowan bypassing or shearing between the precipitates and dislocations (Ma et al., 2014). In L-PBF 316LSS, these nano-particles were reported to be amorphous (Salman et al., 2019), and thus dislocations have to transmit the particles via Orowan bypassing mechanism (Ma et al., 2014), as in oxide dispersion strengthened (ODS) steels (Yu et al., 2013). In our previous work, the strengthening component from the nano-precipitates is about 12.5 MPa, which is negligibly small and in line with the prediction by Ref. (Smith et al., 2019a; Wang et al., 2018). Compared with ODS austenitic stainless steel reinforced by oxide inclusions (about 10 nm diameter), the precipitate dimensions in the present L-PBF 316LSS are significantly larger, and thus lacks effective strengthening effect. Furthermore, the average spacing (1.459  $\mu\text{m}$ ) of nano-particles on the slip plane in our work (Cui et al., 2021b) is much larger than that of typical ODS steels, which further limits the strengthening effect. In recent studies, some measures have been taken to further enhance the strengthening effect of the nano-precipitates in AM alloys (AlMangour et al., 2016; Wang et al., 2020; Wu et al., 2018), such as adding interstitial atoms to the pre-alloyed powder to generate more nano-precipitates on the cell walls without causing defects (Kim et al., 2021). This research field is at the forefront of AM development but little is yet known, and we will focus on this area in our near future work.

Different from the ripple-shaped grains with highly serrated GBs in L-PBF 316LSS, the microstructure of the conventional counterpart in Fig. 4h consists of faceted morphology grains with a high proportion of annealing twin boundaries (see Fig. 3b2). In addition, a low-density of dispersed precipitates were observed in the grain interiors. The SEM-EDS maps in Fig. 4i confirmed that these precipitates were rich in Mo and Mn. The size distribution of them also had been counted and shown in Fig. 4k, ranging from 250 to 2000 nm, with an average value of  $665 \pm 242$  nm, which is significantly larger than the typical shearable particles (Gladman, 1999). Hence, dislocations are inevitably bypass the precipitates for deformation to proceed and the corresponding strength component ( $\sigma_D$ ) could be obtained as follows:

$$\sigma_D = \frac{Gb}{L - d_p} \quad (2)$$

$$L = \sqrt{\frac{2\pi}{3f_l}} R_l \quad (3)$$

where  $G = 73$  GPa and  $b = 0.25$  nm are the shear modulus and the magnitude of Burgers vector for 316LSS.  $L = 15.14$   $\mu\text{m}$ , calculated from Eq. (3), is the average spacing of the precipitates on the glide plane.  $d_p$  is the average size of the precipitates.  $f_l = (0.101 \pm 0.002)\%$  is the concentration of the precipitates in volume.  $R_l = 1/2d_l = 333$  nm is the average radius of the precipitates. Accordingly, the dispersion strengthening in the W316LSS yields a small value of 1.21 MPa. Therefore, these precipitates appear to have very limited impacts on the mechanical properties of the W316LSS.

### 3.3. Effects of the unique microstructural characteristics on the hardness and slip pattern analysis

To reveal the effects of the unique microstructure in L-PBF 316LSS on the dislocation motion during deformation, indentation tests

were performed on the two samples. It is well-known that the microindentation test can give the realistic bulk response of large-area grains affected by the applied load, which means that the microhardness can balance the variations of characteristics in the microstructures. On the contrary, the nanoindentation tests can provide the response of a specific location or a limit area of grains, so this measurement is usually associated with the response of a specific microstructure characteristic or an individual phase. In our study, due to the structural and chemical heterogeneity of L-PBF 316LSS across multiple length scales (Fig. 2 and Fig. 5), the microindentation tests have been adopted, with the aim to get good statistical results. Fig. 5a shows the probability distribution analysis of the microhardness tests in the two samples, which is about  $1.629 \pm 0.070$  GPa for the W316LSS in contrast to  $2.589 \pm 0.116$  GPa for the L-PBF one. This result confirms that the hardness of L-PBF 316LSS with a unique microstructure has increased by approximately 60%.

In order to further compare the resistance to dislocation motion from different microstructures in the two samples, the slip pattern analyses were carried out on the grains with the same orientation from the two samples. One example is shown in Figs. 5b and 5e, where the  $\langle 111 \rangle$  orientation normal to the sample surface was chosen. SEM micrographs in Figs. 5c and 5f show the corresponding residual impressions surrounded by slip steps for the L-PBF and wrought 316LSS, respectively. From the overall appearance of the indentations, the slip patterns were very similar and repeatable, illustrating that the morphologies of these patterns are mainly determined by the crystal orientation of indented grains (Nibur and Bahr, 2003). From the magnified SEM micrographs in Figs. 5d and 5g, the configuration of individual slip steps in the two samples are different in density and characteristics. As reported by Ref. (Nibur and Bahr, 2003), the characteristic of the slip steps contains the slip mode information (wavy and planar slip) of the specific alloy. In our work, compared with the curved slip patterns in the wrought counterpart (see Fig. 5g), the slip steps in L-PBF sample are significant straighter (Fig. 5d), which implies that planar slip may be activated in the L-PBF 316LSS while wavy slip in the W316LSS. Based on the calculations in our previous work, the stacking fault energy (SFE) of the present L-PBF 316LSS is around  $38 \text{ mJ/m}^2$  (Cui et al., 2021a), which is consistent with the previous results analyzed by TEM and neutron diffraction in the wrought 316LSS (Woo et al., 2020). Therefore, the activation of different slip modes in the two samples appears not caused by the SFE, but by the difference in microstructures, and more detailed discussions will be exhibited in Section 4.2. The second difference of the slip steps is the density. Slip steps are the result of the activated dislocations escaping from sample interiors to the free surfaces, and their directions are consistent with the intersection between the glide planes and surface planes. The slip patterns in the L-PBF 316LSS are notably sparser than those in the wrought counterpart. This indicates that the L-PBF 316LSS with unique microstructures, especially the cell structure composed

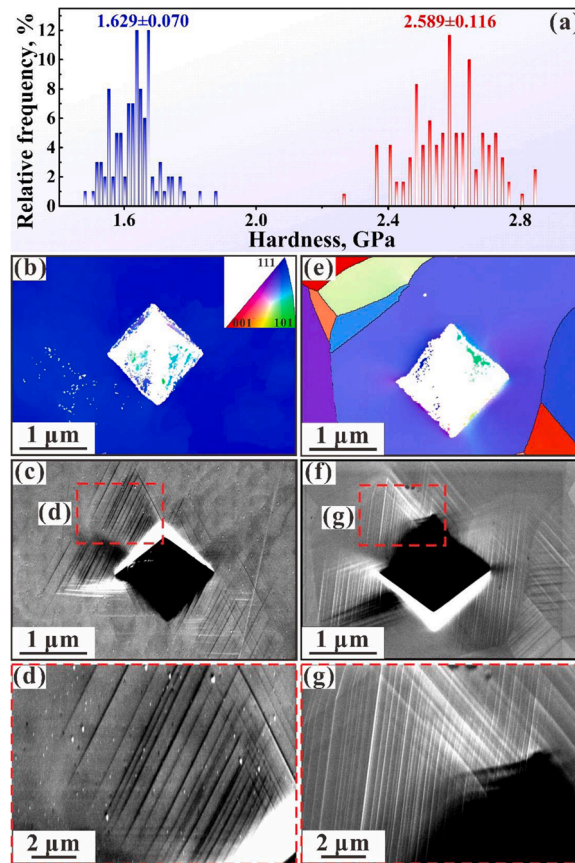


**Fig. 5.** (a) The hardness distribution of the L-PBF and wrought 316LSS respectively, showing that 316LSS is notably strengthened by the unique microstructural characteristics. (b)-(d) and (e)-(g) EBSD IPF maps, indentations and slip traces from the grains with the sample surfaces parallel to (111) planes for L-PBF and wrought 316LSS, respectively.



of tangled dislocations and segregation of the alloying elements, has a much higher resistance to dislocation motion than that of the W316LSS. In other words, the activated dislocations in the L-PBF 316LSS need to overcome great difficulties during the sliding process before they can finally escape to the surface.

In conclusion, due to the difference in the microstructural characteristics, the activated slip modes during deformation is tailored, which in turn enhances the resistance to dislocation motion, and ultimately leads to the improvement of the microhardness.

### 3.4. Comparison of fatigue properties between L-pbf and wrought 316LSS

The S-N curves in Fig. 6a reveal that the L-PBF 316LSS possesses significantly better fatigue properties than the wrought samples. For example, a lifetime of 1,166,607 cycles was obtained for the L-PBF 316LSS under the stress range ( $\Delta\sigma$ ) of 748 MPa. On the contrary, the W316LSS manufactured by the conventional approach shows a fatigue life of 15,616 cycles under a lower  $\Delta\sigma$  of 533 MPa. Note that prior to the deformation all fatigue samples have been carefully mechanically polished to a surface roughness of 0.2  $\mu\text{m}$ . Hence, it is reasonable to consider that the difference in fatigue performance of the two materials is mainly caused by the corresponding microstructures. On the other hand, as indicated by the red lines in Fig. 6a, L-PBF 316LSS appears to have more advantages than W316LSS in the low cycle fatigue (LCF) region, which will be discussed in detail in Section 4.1. Figs. 6b and 6c show the comparison of the total and plastic strain range of both materials as a function of the applied stress range. L-PBF 316LSS exhibits much lower total strain responses than the wrought counterpart. Similar trend is also confirmed by the plastic strain response in Fig. 6c, which suggests that the L-PBF 316LSS exhibits better fatigue resistance due to its unique microstructures. Fig. 6d shows a summary of the cyclic stress range corresponding to the fatigue life of  $10^6$  cycles for different austenitic stainless steels, including our work, wrought 316LSS, L-PBF 316LSS in Ref. (Zhang et al., 2019), and the conventional coarse-grained (CG) 301LN SS (Hamada and Karjalainen, 2010). This further confirms that the present L-PBF 316LSS has a much better fatigue property compared with conventional and previous AM counterparts.

### 3.5. Effects of the unique microstructural characteristics on the crack initiation and propagation behavior

According to the fracture characteristics, the failure process of all the samples roughly consists of the crack initiation, propagation and the tensile overload stages, as the examples shown in Figs. 7a1 and 7b1. The blue lines were applied to distinguish the region of tensile overload stage from the propagation one, and the red dotted double arrows in the same SEM micrographs indicated the lengths of crack propagation, that is, the distance from the crack initiation sites to the borders of the propagation regions. Under this definition,

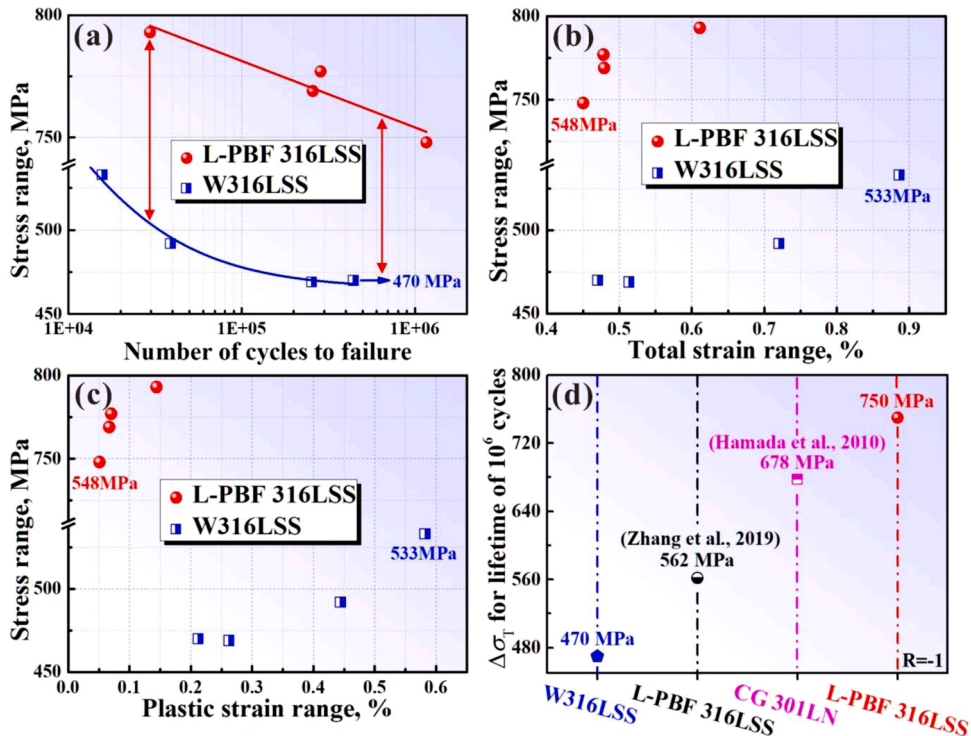
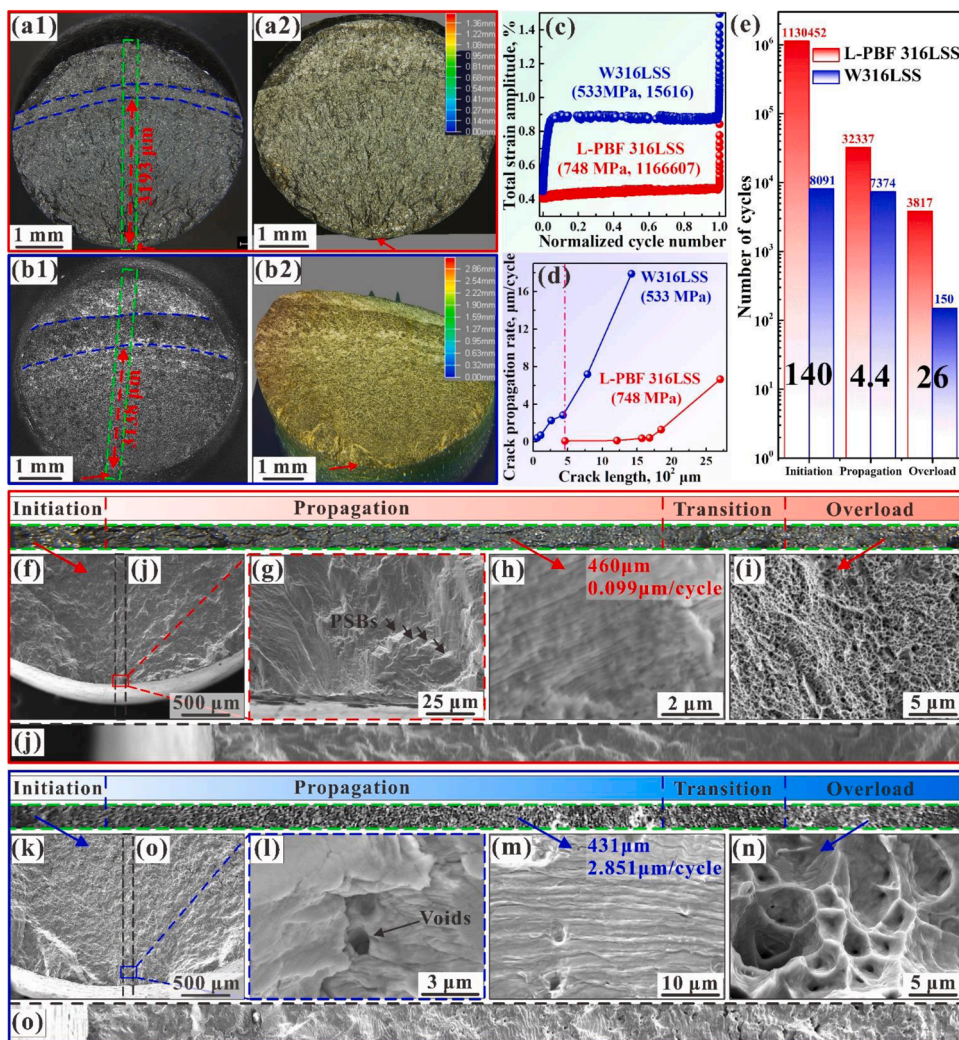


Fig. 6. (a) S-N curves of the L-PBF and wrought 316LSS. (b) Total strain range as a function of applied stress range for the two samples. (c) Plastic strain range versus applied stress range curves for the two samples. (d) Comparison of the total stress range with other austenitic stainless steels under the lifetime of  $10^6$  cycles.



the crack propagation length for the L-PBF and wrought 316LSS were measured to be about 3193 and 3138  $\mu\text{m}$ , respectively. On the other hand, from the overview of the fracture surfaces, more severe necking occurred in the wrought sample (Fig. 7b1), indicating the formation of greater strain localization. This can also be confirmed by the three-dimensional illustration of the fracture surfaces in Figs. 7a2 and 7b2, where the height difference in the wrought sample is significantly greater. Figs. 7f-7i and Figs. 7k-7n show the fracture features of the two samples. The region of the crack initiation was characterized by a relatively flat region without striations, see Figs. 7g and 7l, whereas the propagation and the tensile overload areas were featured by the round ribbon striations (see Figs. 7h and 7m) and ductile dimples (see Figs. 7i and 7n), respectively. Fig. 7g shows the crack initiation site for the L-PBF sample, and no obvious defects (such as micropores and precipitates) that cause crack initiation were observed, but some persistent slip bands were present, which indicates that the dislocation behavior may play a crucial role in crack initiation during the fatigue deformation. Conversely, the crack initiation in the wrought counterpart was due to the subsurface micropores, as shown in Fig. 7l, which was consistent with the previous reports in conventional alloys (Liu et al., 2020b). Another interesting finding of W316LSS is that with the crack length increasing, the size of the micropores on the fracture surface also increases, as shown in Fig. 7o, implying that the dislocation activity may also be important for the crack initiation and propagation in the wrought counterpart.

In order to further illustrate the influence of unique microstructure characteristics on the fatigue behavior of L-PBF 316LSS, we conducted a semi-quantitative analysis of the fracture surfaces for the two representative samples, namely the L-PBF sample under the



**Fig. 7.** (a1) and (b1) Fracture surfaces and the corresponding crack propagation lengths of the L-PBF and wrought 316LSS under  $\Delta\sigma$  of 748 MPa and 533 MPa, respectively. (a2) and (b2) 3D overview of the fracture surfaces in Figs. 7a1 and n 7b1, showing that the distinct necking and severe stress concentration occurred in the W316LSS sample. (c) Total strain response as a function of normalized cycle number for the samples in Figs. 7a1 and 7b1. (d) Relationship between the crack propagation rate and crack length for the two samples. (e) Comparison of the cycle number for the two samples at different fatigue stages. (f)-(i) and (k)-(n) Fracture characteristics at different fatigue stages of the L-PBF and wrought 316LSS in Figs. 7a1 and 7b1, respectively. (j) and (o) Magnified fracture surfaces in the black boxes in Figs. 7f and 7k respectively, showing that the size of the microvoids gradually increases with the crack length increasing in the W316LSS during the fatigue deformation.

$\Delta\sigma$  of 748 MPa and the wrought counterpart under the  $\Delta\sigma$  of 533 MPa. From Fig. 7c, W316LSS exhibits significantly higher strain response and lower lifetime, illustrating its weak fatigue resistance. By measuring the spacing between the striations along the crack propagation direction, the relationship between the propagation rate and crack length of the two samples can be obtained. As shown in Fig. 7d, the rate gradually increases from the lowest value of 0.0987 and 0.10987  $\mu\text{m}/\text{cycle}$  for the L-PBF and wrought 316LSS respectively, and the propagation rate of the W316LSS is much higher than that of the L-PBF 316LSS at any crack length, like a comparison in Figs. 7h and 7m. This difference may be due to the chemical segregation effect combined with dislocation structures in L-PBF 316LSS, which provides greater crack propagation resistance during fatigue deformation. Moreover, from Fig. 7c, the sharp increase of strain near the end of the fatigue process corresponds to the tensile overload stage, which is about 3817 and 150 cycles for the L-PBF and wrought samples, respectively. On the other hand, based on the crack propagation length and the lowest rate, the theoretical maximum number of cycles in the propagation region can be determined to be 32,337 and 7374 cycles for the L-PBF and wrought samples, respectively. Finally, the cycles of the crack initiation stage can be obtained as 1,130,452 and 8091 cycles for the L-PBF and wrought samples, respectively. The summary of the number of cycles at each stage is shown in Fig. 7e, and the black numbers represent the ratio of the cycles for the two samples at each stage. It can be seen that the fatigue process of the L-PBF sample is mainly determined by the crack initiation stage, while the wrought sample is mainly composed of the crack initiation and propagation stages, which agrees well with the above speculation that dislocation activity plays an important role in the corresponding fatigue stages for the two samples. From the black numbers in Fig. 7e, it can be also concluded that the unique microstructure characteristics of L-PBF 316LSS improve its fatigue performance mainly by inhibiting the initiation of microcracks.

#### 4. Discussion

According to the above analysis, the fatigue performance of the present two 316LSS is highly determined by the difference of microstructures and the dislocation behavior, and thus we will have a detailed discussion from these two aspects.

##### 4.1. Influence of the initial microstructure on fatigue performance of the two materials

The excellent fatigue property of the present L-PBF 316LSS comes from its unique microstructure characteristics, such as cell structures, bimodal grain structure and highly serrated GBs. In the light of the microstructural description in Sections 3.1 and 3.2, the yield strength ( $\sigma_y$ ) of 316LSS can be determined by the following equation (Cui et al., 2021b):

$$\sigma_y = \sigma_0 + \sigma_D + \sigma_{SS} + \sigma_{GB} + \sigma_{Dis} \quad (4)$$

where  $\sigma_0$  is the friction stress, which is a constant for the two materials.  $\sigma_D$  is the dispersion strengthening generated from the interaction between dislocations and the small amount of the precipitates,  $\sigma_{SS}$  is the solid solution strengthening induced by the difference in size and shear modulus of solute atoms and matrix atoms,  $\sigma_{GB}$  is the grain boundary strengthening described by the Hall–Petch relation,  $\sigma_{Dis}$  is the dislocation strengthening. In Section 3.2, the values of  $\sigma_D$  were calculated to be 12.5 and 1.21 MPa for the L-PBF and wrought 316LSS respectively, and thus their differences can be ignored. In addition, due to the extremely low content of the precipitates (0.399% in L-PBF 316LSS and 0.101% in wrought 316LSS), the composition of matrix is basically not affected, hence the difference in  $\sigma_{SS}$  between the two materials does not seem to be large. Since the L-PBF 316LSS is composed of columnar grains, we use the geometric mean of 18.71  $\mu\text{m}$  to represent the microstructure-averaged grain size in the further calculation. Therefore,  $\sigma_{GB}$  for the two materials can be estimated as follows (Cui et al., 2021b):

$$\sigma_{GB} = \frac{k_y}{\sqrt{d_G}} \quad (5)$$

where  $k_y = 452 \text{ MPa}/\mu\text{m}^{1/2}$  is the strengthening coefficient for 316LSS (Huang et al., 2011).  $d_G$  is the average grain size. Consequently, the strengthening component resulting from the grain-size refinement for L-PBF and wrought 316LSS were determined to be about 106 MPa and 111 MPa respectively, but gives a negligible difference in strength. This means that the difference in dislocation density should be responsibility for the strength difference between the two materials. A high density of dislocations will be introduced in the obtained components because of the ultra-fast cooling rate during the AM process, which undoubtedly affects the corresponding mechanical properties. For metallic materials, the dislocation strengthening is one of the most rudimentary strengthening strategy and usually described by the Bailey–Hirsch relation as follows (Liu et al., 2020a):

$$\sigma_{Dis} = M\alpha Gb\sqrt{\rho} \quad (6)$$

where  $M$  is the Taylor factor, and the corresponding values for L-PBF and wrought 316LSS are determined to be 3.11 and 2.91 respectively from the EBSD-acquired data.  $G = 73 \text{ GPa}$  is the shear modulus of 316LSS (Yin et al., 2019).  $b$  is the magnitude of Burgers vector, and its value is 0.258 nm for 316LSS (Lee and Chiu, 2006).  $\alpha$  is an empirical constant related to the dislocation configuration in the microstructure. For the homogeneously distributed dislocations (like the W316LSS), the value of  $\alpha$  is taken as 0.3 (Cui et al., 2021b), while  $\alpha = 0.23$  for the microstructure consisting of cell-like dislocation structures (like the L-PBF 316LSS) (He et al., 2017).  $\rho$  is the total dislocation density, which is the summed density of the GNDs and statistically stored dislocations (SSDs). On the basis of the previous reports (Cui et al., 2021b; Muránsky et al., 2019; Zhu et al., 2018), most of the dislocations in FCC crystals are composed of GNDs. Therefore, we can use the EBSD-acquired GND density in Section 3.1 to evaluate the dislocation strengthening in the two

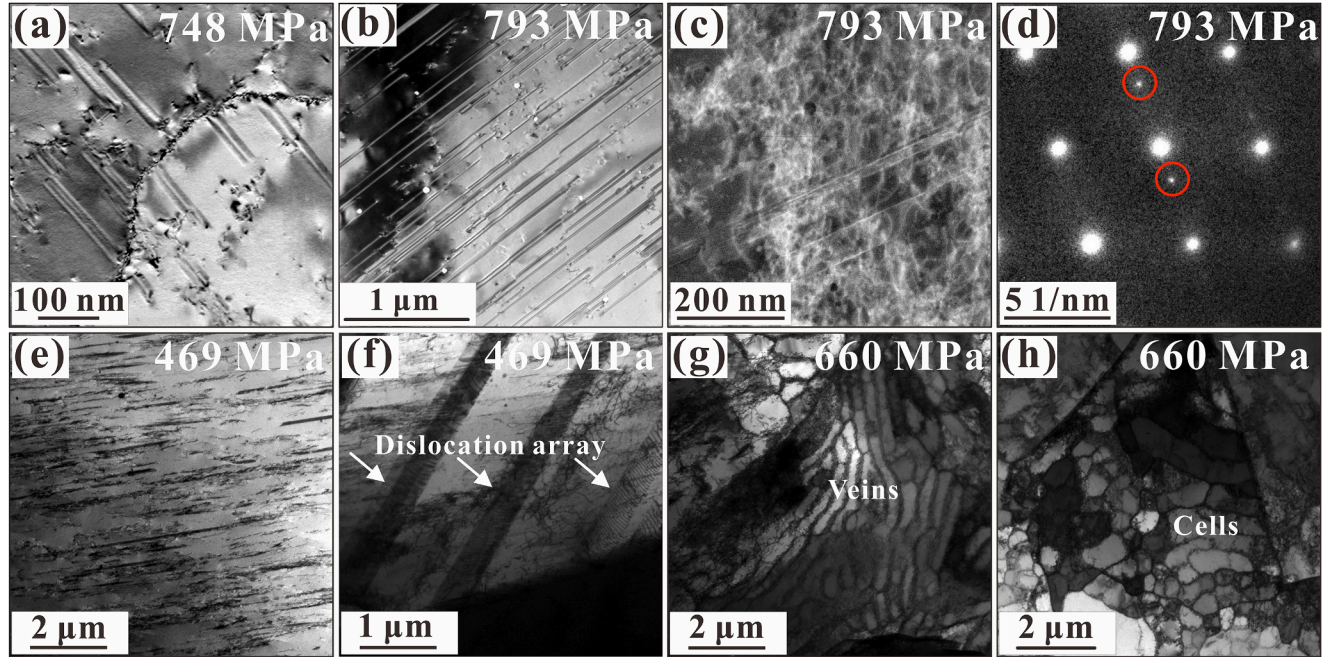


**Fig. 8.** Typical dislocation configurations of L-PBF (a)-(d) and wrought (e)-(h) 316LSS after failure at different  $\Delta\sigma$ . (d) The SAED pattern of deformation twins in Fig. 8c. Values of  $\Delta\sigma$  were listed on the upper right corner of the corresponding images.



materials, and a total strength increment of 360 MPa and 195 MPa was obtained for the L-PBF and wrought 316LSS. Moreover, the dislocation strengthening gives a strength difference of 165 MPa, which is evidently higher than that of the other mechanisms. Therefore, it can be inferred that the pre-existing high density dislocations increase the strength of L-PBF alloys by suppressing the movement of dislocations in the plastic deformation. Furthermore, the numerous pre-existing dislocations pinned by the segregated atoms on the cell walls can increase the critical stress required for strain localization during cyclic deformation, thereby prolonging the fatigue life. This can be verified by the more severe necking of the W316LSS fracture surface in Figs. 7b1 and 7b2.

In addition to the dislocation density, the dislocation configuration, namely the distribution of dislocations in the microstructure, also has a certain impact on the dislocation motion, which in turn affects the fatigue performance. In the microstructure of L-PBF 316LSS, as shown in Fig. 4e, dislocations are tangled on the cell walls to form cell structures, rather than randomly distributed. From values of the empirical constant  $\alpha$  in Eq. (6), it can be speculated that the homogeneously distributed dislocation structure contributes slightly more to the strength enhancement of metallic materials than the cell-like dislocation structure. Note that the cell structure in the present L-PBF 316LSS is different from the cell-like dislocation structure in the deformed conventional alloys, since they are pinned by the segregated atoms on the cell walls, which may increase the drag force for dislocation motion (Wang et al., 2018). Hence, the strength contribution from the different configurations of dislocations may not be much different. However, one notable feature of the unique cell structure in AM alloys is that it can alter the dislocation behavior during plastic deformation, such as promoting the decomposition of perfect dislocations into extended dislocations and slowing down the dislocation motion, thereby significantly improving the ductility of AM alloys (Liu et al., 2018). To the best of our knowledge, this behavior has never been reported in the uniformly distributed dislocation configurations. On the other hand, it is generally accepted that the high-cycle fatigue (HCF) properties of metallic materials mainly correlate with the material's strength, while the LCF properties are determined by the material's ductility (Mughrabi and Höppel, 2010). Therefore, the cell-like dislocation structure in L-PBF 316LSS appears to have a more positive effect on LCF performance, which seems to be confirmed by the fatigue results marked by the red lines in Fig. 6a.

Apart from the dislocation strengthening, other microstructure characteristics, such as bimodal grain structure and cell structures may also play a role for the fatigue performance of L-PBF 316LSS. It is widely accepted that heterogeneous microstructure can induce high back stress during deformation, which significantly inhibits the movement of dislocations (Kong et al., 2020). In our case, as shown in Fig. 2, unlike the uniform grains in W316LSS, the microstructure of L-PBF 316LSS consists of large-sized  $\langle 101 \rangle$  oriented grains and small-sized  $\langle 001 \rangle$  oriented grains. Hence, remarkable back stress was considered to be generated in the L-PBF 316LSS during cyclic deformation (Kong et al., 2020), thereby relieving strain localization and improving the fatigue resistance. Furthermore, the cell structures would also undergo a non-ignorable hetero-deformation-induced stress effect under plastic deformation (Kong et al., 2020), which suppressed the dislocation motion and played a part in the excellent fatigue property. Another important feature of L-PBF 316LSS is the chemical microsegregation within cell structures (see Figs. 4f–4g), which may also generate non-negligible resistance to dislocation motion (Ding et al., 2020; Smith et al., 2019a; Sun et al., 2021). Traditionally, when it comes to chemical heterogeneity, it is considered as a detrimental effect, and should be avoided or eliminated. For example, the element segregation in casting nickel-based superalloys often requires high-temperature homogenization treatment to guarantee their properties (Blaizot et al., 2016; Cui et al., 2018; Huang et al., 2008; León-Cázarez et al., 2020; Nganbe and Heilmaier, 2009). However, recent studies indicated that the chemical heterogeneity in small-scale can be an effective method to enhance the mechanical properties of metallic materials (Ding et al., 2020; Sun et al., 2021), e.g., by introducing hundreds of nanometer-scale Mn segregation islands into the microstructure, the failure elongation of high-strength steels in hydrogen-containing environments was significantly increased from 15% to 30% (Sun et al., 2021). Similar results were also revealed by Ding et al. (Ding et al., 2020) that after introducing a unique chemical boundary with a few nanometers in thickness into plain steels, the failure elongation was increased from 15% to 20% accompanied with a strength increment of 600 MPa. In the present work, as shown in Figs. 4f–4g, Cr and Mo were segregated along the cell walls, and the cell size is around 530 nm, therefore the small-scale chemical microsegregation indeed existed in the cell structures. The study by Thale R. Smith et al. (Smith et al., 2019a) confirmed that 28% of the yield strength of AM 304LSS was contributed by the microsegregation strengthening, which mainly comes from the coherent internal stresses and the spatial variation of the elastic modulus between the enriched regions (cell walls) and depleted regions (cell interiors) (Kato et al., 1980). Therefore, the chemical microsegregation does have certain impacts on the movement of dislocations during plastic deformation, but more work is needed for the further study. In conclusion, the pre-existing high-density dislocations together with the unique microstructure characteristics including bimodal grain structure, cell structures and chemical microsegregation are considered to be the reasons that L-PBF 316LSS has better fatigue performance than the wrought counterpart. The unique cell structure can notably improve the ductility of metallic materials, therefore it seems to have a more positive effect on LCF performance of L-PBF 316LSS.

#### 4.2. Influence of the deformation mechanism on fatigue performance of the two materials

The fatigue performance of a material is related to its microstructure evolution during the cyclic loading (Cui et al., 2020). Detailed deformation mechanism analyses were conducted on the two materials under different testing conditions to investigate their fatigue behavior, as illustrated in Fig. 8. The bright-field TEM micrographs in Figs. 8a–8d show that the typical dislocation substructures in the post-deformed L-PBF 316LSS consist of slip bands (not shown here), stacking faults and deformation twins, and it appears that with the cyclic stress increases higher density of stacking faults are formed. From Figs. 8a–8c, it can be seen that although large populations of deformation twins cut through the cell structures, the configurations of them are preserved, which proves that the cells have excellent mechanical stability. Different from the planar dislocation substructures in L-PBF 316LSS, the most prominent substructures in the post-deformed W316LSS are slip bands (Figs. 8e–8f) and low-energy structures, namely the high dislocation density walls accompanied with low dislocation density channels (Figs. 8g–8h). According to the morphology, the planar slip bands can be divided in two types.



One is composed of tangled dislocations, as illustrated in Fig. 8e, and the other is formed by the parallel dislocation arrays, as shown in Fig. 8f. On the other hand, by comparing Figs. 8e–8f and Figs. 8g–8h, the dislocation substructures change from the planar slip bands under low  $\Delta\sigma$  of 469 MPa to the vein-/cell-like structures under high  $\Delta\sigma$  of 660 MPa, illustrating the activated slip mode transition from planar to wavy slip as the cyclic stress increases.

Based on the above investigations, the different dislocation behaviors observed in L-PBF and wrought 316LSS provide insights into the differences in their fatigue properties. It is clear that the planar dislocation substructures, such as stacking faults and deformation twins, are dominantly observed in L-PBF 316LSS, whereas the frequent dislocation substructures in W316LSS are the localized slip bands and wavy vein-/cell-like structures. As mentioned in Section 3.3, the SFE of the two materials are similar, hence the distinct dislocation behaviors in these two materials appear to be caused by the microstructures, especially the unique cell structures with the accompanying segregation of the alloying elements in L-PBF 316LSS.

Recent studies shows that compared with the widely accepted SFE, the generalized stacking fault energy (GSFE) is more appropriate to properly classify the deformation modes of metallic materials (Yamakov et al., 2004, 2002). For FCC crystal, GSFE represents the energy dependency of the rigidly sheared crystal within the  $\{1\ 1\ 1\}$  plane along the  $\langle 112 \rangle$  direction (Li et al., 2014b). In our work, from the TEM micrographs of the post-deformed L-PBF 316LSS in Fig. 8, basically all stacking faults are initiated from the cell walls. Therefore, the segregation of Mo and Cr on the cell walls might reduce the GSFE of L-PBF 316LSS and result in the activation of planar deformation mechanisms. On the other hand, the formation of stacking faults can be rationalized as follows. When a perfect dislocation, consisting of a pair of Shockley partial dislocations and a stacking fault (Cui et al., 2022a), moves through the cell walls, the segregated atoms would produce a drag force on the partial dislocation based on the Suzuki effect (Kaneko et al., 1995). When the external stress was high enough, a leading partial was emitted from the cell wall. At this moment, the trailing partial was still trapped by the cell wall. If the trailing partial was pinned by the cell wall forever, then the stacking faults can be formed in the L-PBF 316LSS. Actually, this process has been confirmed by the in-situ TEM analysis on L-PBF 316LSS in Ref. (Liu et al., 2018). Furthermore, it could be speculated that the deformation twins formed as the partial dislocations with the same Burgers vector glided on the adjacent planes. More work needs to be done on the relationship between the chemical segregation on the cell walls and GSFE, but this is beyond the scope of the present work, and will be part of a more detailed study in our future investigation.

The wavy vein-/cell-like structures in W316LSS are related to the generation of extrusion and intrusion on the sample surface, where fatigue cracks tend to nucleate (Mughrabi, 2009). In addition, the localized slip bands are also known to be the initiation sites for fatigue microcracks (Li et al., 2014a). Contrarily, the planar dislocation substructures in L-PBF 316LSS, in particular the deformation twins, can delay the strain localization and restrain slip band generation, thereby inhibiting crack initiation and promoting the greater fatigue resistance of L-PBF 316LSS. In conclusion, the enhanced planar slip by its unique microstructures in L-PBF 316LSS also plays an additional role in the excellent fatigue property.

## 5. Conclusion

- (1) The as-built PBF 316LSS shows a pronounced heterogeneity, not only structural but also chemical, with a unique microstructure of semi-elliptical MPBs, highly serrated GBs, bimodal grain structure, nano-precipitates, solidification cell structures, and chemical segregations. However, the microstructure of wrought and solution annealed 316LSS consists of uniform faceted grains with a small amount of dispersed precipitates in the grain interiors.
- (2) Due to the unique microstructure, the microhardness of L-PBF 316LSS reaches  $2.589 \pm 0.116$  GPa, which is about 1.6 times that of W316LSS. Compared with the curved slip steps in W316LSS, the slip steps in the L-PBF sample are significantly straighter, indicating that the planar slip appeared to be activated in L-PBF 316LSS, while the wavy slip in W316LSS. In addition, the sparser slip steps of L-PBF 316LSS revealed its greater dislocation storage capability.
- (3) Semi-quantitative analyses of fracture surfaces revealed that the fatigue process of L-PBF 316LSS was dominated by the crack initiation stage, while the wrought counterpart is primarily composed of the crack initiation and propagation stages. Furthermore, by strongly suppressing the crack initiation stage, the unique microstructure characteristics notably improved the fatigue performance of L-PBF 316LSS.
- (4) The fatigue performance of L-PBF 316LSS was significantly better than that of W316LSS due to its unique microstructure characteristics, including the pre-existing high-density dislocations, bimodal grain structure, cell structures and chemical microsegregation. Furthermore, the planar dislocation substructures generated during the cyclic deformation process, especially the deformation twins, also made a positive contribution to its greater fatigue resistance. The unique cell structure appears to be more effective in improving the LCF performance of L-PBF 316LSS due to the enhanced ductility.

## Author statement

Luqing Cui carried out the manufacturing processing of the alloys, structural analyses using TEM, SEM, EBSD and the mechanical property analyses. Fuqing Jiang and Zhiqing Yang carried out the TEM investigations. Johan Moverare, Ru Lin Peng and Reza Taherzadeh Mousavian designed the experimental program and Johan Moverare coordinated the overall project. All authors contributed to the interpretation of the results and to the writing of the paper.

## Declaration of Competing Interest

The authors declare that they have no conflict of interests or personal relationships that could have appeared to influence the work

reported in this paper.

## Acknowledgements

This study is supported by the Swedish Governmental Agency for Innovation Systems (Vinnova grant 2016–05175) and the Center for Additive Manufacturing-metal (CAM<sup>2</sup>). This research is also supported in part by a research grant from Science Foundation Ireland (SFI) under Grant Number 16/RC/3872 and is cofounded under the European Regional Development Fund and by the I-Form industry partners. Also, the assistance of staff and technicians in Dublin City University and Waterford Institute of Technology is acknowledged. ZY thanks Ji Hua Laboratory for financial support, X210141TL210.

## References

- AlMangour, B., Grzesiak, D., Jenn, M., 2016. Selective laser melting of TiC reinforced 316L stainless steel matrix nanocomposites: influence of starting TiC particle size and volume content. *Mater. Des.* 104, 141–151.
- AlMangour, B., Kim, Y.K., Grzesiak, D., Lee, K.A., 2019. Novel TiB<sub>2</sub>-reinforced 316L stainless steel nanocomposites with excellent room- and high-temperature yield strength developed by additive manufacturing. *Compos. B. Eng.* 156, 51–63.
- Andreau, O., Pessard, E., Koutiri, I., Peyre, P., Saintier, N., 2021. Influence of the position and size of various deterministic defects on the high cycle fatigue resistance of a 316L steel manufactured by laser powder bed fusion. *Int. J. Fatigue* 143, 105930.
- Birosca, S., Liu, G., Ding, R., Jiang, J., Simm, T., Deen, C., Whittaker, M., 2019. The dislocation behaviour and GND development in a nickel based superalloy during creep. *Int. J. Plast* 118, 252–268.
- Blaizot, J., Chaise, T., Nélis, D., Perez, M., Cazottes, S., Chaudet, P., 2016. Constitutive model for nickel alloy 690 (Inconel 690) at various strain rates and temperatures. *Int. J. Plast.* 80, 139–153.
- Bronkhorst, C.A., Mayeur, J.R., Livescu, V., Pokharel, R., Brown, D.W., Gray, G.T., 2019. Structural representation of additively manufactured 316L austenitic stainless steel. *Int. J. Plast* 118, 70–86.
- Cao, Y., Moumni, Z., Zhu, J., Zhang, Y., You, Y., Zhang, W., 2020. Comparative investigation of the fatigue limit of additive-manufactured and rolled 316 steel based on self-heating approach. *Eng. Fract. Mech.* 223, 106746.
- Cherry, J.A., Davies, H.M., Mehmood, S., Lavery, N.P., Brown, S.G.R., Siens, J., 2015. Investigation into the effect of process parameters on microstructural and physical properties of 316L stainless steel parts by selective laser melting. *Int. J. Adv. Manuf. Technol.* 76, 869–879.
- Cui, L., Deng, D., Jiang, F., Peng, R.L., Xin, T., Mousavian, R.T., Yang, Z., Moverare, J., 2022a. Superior low cycle fatigue property from cell structures in additively manufactured 316L stainless steel. *J. Mater. Sci. Technol.* Accepted.
- Cui, L., Jiang, F., Deng, D., Xin, T., Sun, X., Mousavian, R.T., Peng, R.L., Yang, Z., Moverare, J., 2021a. Cyclic response of additive manufactured 316L stainless steel: the role of cell structures. *Scr. Mater.* 205, 114190.
- Cui, L., Jiang, S., Xu, J., Peng, R.L., Mousavian, R.T., Moverare, J., 2021b. Revealing relationships between microstructure and hardening nature of additively manufactured 316L stainless steel. *Mater. Des.* 198.
- Cui, L., Liu, J., Peng, R.L., Yu, J., Moverare, J., Sun, X., 2020. Low cycle fatigue behavior and microstructural evolution of nickel-based superalloy M951G at elevated temperatures. *Mater. Charact.* 163, 110241.
- Cui, L., Yu, C.-H., Jiang, S., Sun, X., Peng, R.L., Lundgren, J.-E., Moverare, J., 2022b. A new approach for determining GND and SSD densities based on indentation size effect: an application to additive-manufactured Hastelloy X. *J. Mater. Sci. Technol.* 96, 295–307.
- Cui, L., Yu, J., Liu, J., Sun, X., 2018. Microstructural evolutions and fracture behaviors of a newly developed nickel-base superalloy during creep deformation. *J. Alloys Compd.* 746, 335–349.
- Cunningham, R., Zhao, C., Parab, N., Kantzos, C., Pauza, J., Fezzaa, K., Sun, T., Rollett, A.D., 2019. Keyhole threshold and morphology in laser melting revealed by ultrahigh-speed x-ray imaging. *Science* 363, 849–852.
- Darvish, K., Chen, Z.W., Pasang, T., 2016. Reducing lack of fusion during selective laser melting of CoCrMo alloy: effect of laser power on geometrical features of tracks. *Mater. Des.* 112, 357–366.
- Das, S., Hofmann, F., Tarleton, E., 2018. Consistent determination of geometrically necessary dislocation density from simulations and experiments. *Int. J. Plast* 109, 18–42.
- Deng, D., Peng, R.L., Moverare, J., 2021. High temperature mechanical integrity of selective laser melted alloy 718 evaluated by slow strain rate tests. *Int. J. Plast* 140, 102974.
- Ding, R., Yao, Y., Sun, B., Liu, G., He, J., Li, T., Wan, X., Dai, Z., Ponge, D., Raabe, D., Zhang, C., Godfrey, A., Miyamoto, G., Furuhashi, T., Yang, Z., van der Zwaag, S., Chen, H., 2020. Chemical boundary engineering: a new route toward lean, ultrastrong yet ductile steels. *Sci. Adv.* 6, eaay1430.
- Elangeswaran, C., Cutolo, A., Muralidharan, G.K., Vanmeensel, K., Van Hooreweder, B., 2020. Microstructural analysis and fatigue crack initiation modelling of additively manufactured 316L after different heat treatments. *Mater. Des.* 194, 108962.
- Gladman, T., 1999. Precipitation hardening in metals. *Mater. Sci. Technol.* 15, 30–36.
- Hamada, A.S., Karjalainen, L.P., 2010. High-cycle fatigue behavior of ultrafine-grained austenitic stainless and TWIP steels. *Mater. Sci. Eng. A* 527, 5715–5722.
- He, B.B., Hu, B., Yen, H.W., Cheng, G.J., Wang, Z.K., Luo, H.W., Huang, M.X., 2017. High dislocation density-induced large ductility in deformed and partitioned steels. *Science* 357, 1029–1032.
- Huang, C.X., Yang, G., Wang, C., Zhang, Z.F., Wu, S.D., 2011. Mechanical behaviors of ultrafine-grained 301 austenitic stainless steel produced by equal-channel angular pressing. *Metall. Mater. Trans. A* 42, 2061–2071.
- Huang, E.W., Barabash, R.I., Wang, Y., Clausen, B., Li, L., Liaw, P.K., Ice, G.E., Ren, Y., Choo, H., Pike, L.M., Klarstrom, D.L., 2008. Plastic behavior of a nickel-based alloy under monotonic-tension and low-cycle-fatigue loading. *Int. J. Plast* 24, 1440–1456.
- Kahlin, M., Ansell, H., Basu, D., Kerwin, A., Newton, L., Smith, B., Moverare, J.J., 2020. Improved fatigue strength of additively manufactured Ti6Al4V by surface post processing. *Int. J. Fatigue* 134, 105497.
- Kaneko, Y., Kaneko, K., Nohara, A., Saka, H., 1995. Evidence for Suzuki effect in an Fe-Ni-Cr austenitic stainless steel. *Philos. Mag. A* 71, 399–407.
- Kato, M., Mori, T., Schwartz, L.H., 1980. Hardening by spinodal modulated structure. *Acta Metall.* 28, 285–290.
- Kim, Y.K., Baek, M.S., Yang, S., Lee, K.A., 2021. In-situ formed oxide enables extraordinary high-cycle fatigue resistance in additively manufactured CoCrFeMnNi high-entropy alloy. *Addit. Manuf.* 38.
- Kim, Y.K., Kim, M.C., Lee, K.A., 2022. 1.45GPa ultrastrong cryogenic strength with superior impact toughness in the in-situ nano oxide reinforced CrMnFeCoNi high-entropy alloy matrix nanocomposite manufactured by laser powder bed fusion. *J. Mater. Sci. Technol.* 97, 10–19.
- Kong, D., Dong, C., Ni, X., Liang, Z., Man, C., Li, X., 2020. Hetero-deformation-induced stress in additively manufactured 316L stainless steel. *Mater. Res. Lett.* 8, 390–397.
- Lee, W.-S., Chiu, C.-C., 2006. Deformation and fracture behavior of 316L sintered stainless steel under various strain rate and relative sintered density conditions. *Metall. Mater. Trans. A* 37, 3685–3696.
- León-Cázarez, F.D., Monni, F., Jackson, T., Galindo-Nava, E.I., Rae, C.M.F., 2020. Stress response and microstructural evolution of nickel-based superalloys during low cycle fatigue: physics-based modelling of cyclic hardening and softening. *Int. J. Plast.* 102682.
- Li, M., Tao, Dai, J.W., Jia, X.J., Gu, X.H., Dai, T., 2020a. Microstructure and mechanical properties of 308L stainless steel fabricated by laminar plasma additive manufacturing. *Mater. Sci. Eng. A* 770.

- Li, P., Li, Q.Q., Jin, T., Zhou, Y.Z., Li, J.G., Sun, X.F., Zhang, Z.F., 2014a. Comparison of low-cycle fatigue behaviors between two nickel-based single-crystal superalloys. *Int. J. Fatigue* 63, 137–144.
- Li, W., Lu, S., Hu, Q.-M., Kwon, S.K., Johansson, B., Vitos, L., 2014b. Generalized stacking fault energies of alloys. *J. Phys.: Condens. Matter* 26, 265005.
- Li, Z., Li, Z., Tan, Z., Xiong, D.-B., Guo, Q., 2020b. Stress relaxation and the cellular structure-dependence of plastic deformation in additively manufactured AlSi10Mg alloys. *Int. J. Plast* 127, 102640.
- Liu, C., Yang, J., Ma, P., Ma, Z., Zhan, L., Chen, K., Huang, M., Li, J., Li, Z., 2020a. Large creep formability and strength–ductility synergy enabled by engineering dislocations in aluminum alloys. *Int. J. Plast* 102774.
- Liu, G., Winwood, S., Rhodes, K., Biroscs, S., 2020b. The effects of grain size, dendritic structure and crystallographic orientation on fatigue crack propagation in IN713C nickel-based superalloy. *Int. J. Plast* 125, 150–168.
- Liu, L., Ding, Q., Zhong, Y., Zou, J., Wu, J., Chiu, Y.-L., Li, J., Zhang, Z., Yu, Q., Shen, Z., 2018. Dislocation network in additive manufactured steel breaks strength–ductility trade-off. *Mater. Today* 21, 354–361.
- Ma, K., Wen, H., Hu, T., Topping, T.D., Isheim, D., Seidman, D.N., Lavernia, E.J., Schoenung, J.M., 2014. Mechanical behavior and strengthening mechanisms in ultrafine grain precipitation-strengthened aluminum alloy. *Acta Mater.* 62, 141–155.
- Maleki, E., Bagherifard, S., Bandini, M., Guagliano, M., 2021. Surface post-treatments for metal additive manufacturing: progress, challenges, and opportunities. *Addit. Manuf.* 37, 101619.
- Mughrabi, H., 2009. Cyclic Slip Irreversibilities and the Evolution of Fatigue Damage. *Metall. Mater. Trans. A* 40, 1257–1279.
- Mughrabi, H., Höppel, H.W., 2010. Cyclic deformation and fatigue properties of very fine-grained metals and alloys. *Int. J. Fatigue* 32, 1413–1427.
- Muránsky, O., Balogh, L., Tran, M., Hamelin, C.J., Park, J.S., Daymond, M.R., 2019. On the measurement of dislocations and dislocation substructures using EBSD and HRSD techniques. *Acta Mater.* 175, 297–313.
- Nabil Bassim, M., Klassen, R.J., 1986. Variation in dislocation cell size with local strain in a low alloy steel. *Mater. Sci. Eng.* 81, 163–167.
- Nakada, N., Ito, H., Matsuoka, Y., Tsuchiyama, T., Takaki, S., 2010. Deformation-induced martensitic transformation behavior in cold-rolled and cold-drawn type 316 stainless steels. *Acta Mater.* 58, 895–903.
- Nayak, S.K., Mishra, S.K., Paul, C.P., Jinoop, A.N., Bindra, K.S., 2020. Effect of energy density on laser powder bed fusion built single tracks and thin wall structures with 100µm preplaced powder layer thickness. *Opt. Laser Technol.* 125, 106016.
- Nganbe, M., Heilmair, M., 2009. High temperature strength and failure of the Ni-base superalloy PM 3030. *Int. J. Plast* 25, 822–837.
- Nibur, K.A., Bahr, D.F., 2003. Identifying slip systems around indentations in FCC metals. *Scr. Mater.* 49, 1055–1060.
- Pakkanen, J., 2018. Designing For Additive Manufacturing-Product and Process Driven Design For Metals and Polymers. Politecnico di Torino, Torino.
- Pantleon, W., 2008. Resolving the geometrically necessary dislocation content by conventional electron backscattering diffraction. *Scr. Mater.* 58, 994–997.
- Paramatmuni, C., Dunne, F.P.E., 2020. Effect of twin crystallographic orientation on deformation and growth in Mg alloy AZ31. *Int. J. Plast* 135, 102775.
- Pegues, J.W., Roach, M.D., Shamsaei, N., 2020. Additive manufacturing of fatigue resistant austenitic stainless steels by understanding process-structure-property relationships. *Mater. Res. Lett.* 8, 8–15.
- Pokharel, R., Patra, A., Brown, D.W., Clausen, B., Vogel, S.C., Gray, G.T., 2019. An analysis of phase stresses in additively manufactured 304L stainless steel using neutron diffraction measurements and crystal plasticity finite element simulations. *Int. J. Plast* 121, 201–217.
- Salman, O.O., Gammer, C., Chaubey, A.K., Eckert, J., Scudino, S., 2019. Effect of heat treatment on microstructure and mechanical properties of 316L steel synthesized by selective laser melting. *Mater. Sci. Eng. A* 748, 205–212.
- Smith, T.R., Sugar, J.D., San Marchi, C., Schoenung, J.M., 2019a. Strengthening mechanisms in directed energy deposited austenitic stainless steel. *Acta Mater.* 164, 728–740.
- Smith, T.R., Sugar, J.D., Schoenung, J.M., San Marchi, C., 2019b. Relationship between manufacturing defects and fatigue properties of additive manufactured austenitic stainless steel. *Mater. Sci. Eng. A* 765, 138268.
- Sun, B., Lu, W., Gault, B., Ding, R., Mäkinen, S.K., Wan, D., Wu, C.-H., Chen, H., Ponge, D., Raabe, D., 2021. Chemical heterogeneity enhances hydrogen resistance in high-strength steels. *Nat. Mater.*
- Sun, S.-H., Hagihara, K., Nakano, T., 2018a. Effect of scanning strategy on texture formation in Ni-25at.%Mo alloys fabricated by selective laser melting. *Mater. Des.* 140, 307–316.
- Sun, Z., Tan, X., Tor, S.B., Chua, C.K., 2018b. Simultaneously enhanced strength and ductility for 3D-printed stainless steel 316L by selective laser melting. *NPG Asia Mater.* 10, 127–136.
- Svensson, M., Ackelid, U., Ab, A., 2010. In: Titanium alloys manufactured with electron beam melting mechanical and chemical properties, Proceedings of the materials and processes for medical devices conference. ASM International, pp. 189–194.
- Wang, H., Zhu, Z.G., Chen, H., Wang, A.G., Liu, J.Q., Liu, H.W., Zheng, R.K., Nai, S.M.L., Primig, S., Babu, S.S., Ringer, S.P., Liao, X.Z., 2020. Effect of cyclic rapid thermal loadings on the microstructural evolution of a CrMnFeCoNi high-entropy alloy manufactured by selective laser melting. *Acta Mater.* 196, 609–625.
- Wang, X., Muñoz-Lerma, J.A., Sanchez-Mata, O., Attarian Shandiz, M., Brodusich, N., Gauvin, R., Brochu, M., 2019. Characterization of single crystalline austenitic stainless steel thin strips processed by laser powder bed fusion. *Scr. Mater.* 163, 51–56.
- Wang, Y.M., Voisin, T., McKeown, J.T., Ye, J.C., Calta, N.P., Li, Z., Zeng, Z., Zhang, Y., Chen, W., Roehling, T.T., Ott, R.T., Santala, M.K., Depond, P.J., Matthews, M.J., Hamza, A.V., Zhu, T., 2018. Additively manufactured hierarchical stainless steels with high strength and ductility. *Nat. Mater.* 17, 63–71.
- Witzen, W.A., Polonsky, A.T., Pollock, T.M., Beyerlein, I.J., 2020. Three-dimensional maps of geometrically necessary dislocation densities in additively manufactured Ni-based superalloy IN718. *Int. J. Plast* 131, 102709.
- Woo, W., Jeong, J.S., Kim, D.K., Lee, C.M., Choi, S.H., Suh, J.Y., Lee, S.Y., Harjo, S., Kawasaki, T., 2020. Stacking fault energy analyses of additively manufactured stainless steel 316L and CrCoNi medium entropy alloy using in-situ neutron diffraction. *Sci. Rep.* 10, 1350.
- Wu, W., Zhou, R., Wei, B., Ni, S., Liu, Y., Song, M., 2018. Nanosized precipitates and dislocation networks reinforced C-containing CoCrFeNi high-entropy alloy fabricated by selective laser melting. *Mater. Charact.* 144, 605–610.
- Yamakov, V., Wolf, D., Phillpot, S., Mukherjee, A., Gleiter, H., 2004. Deformation-mechanism map for nanocrystalline metals by molecular-dynamics simulation. *Nat. Mater.* 3, 43–47.
- Yamakov, V., Wolf, D., Phillpot, S.R., Mukherjee, A.K., Gleiter, H., 2002. Dislocation processes in the deformation of nanocrystalline aluminium by molecular-dynamics simulation. *Nat. Mater.* 1, 45–49.
- Yan, F., Xiong, W., Faierman, E., Olson, G.B., 2018. Characterization of nano-scale oxides in austenitic stainless steel processed by powder bed fusion. *Scr. Mater.* 155, 104–108.
- Yin, Y.J., Sun, J.Q., Guo, J., Kan, X.F., Yang, D.C., 2019. Mechanism of high yield strength and yield ratio of 316 L stainless steel by additive manufacturing. *Mater. Sci. Eng. A* 744, 773–777.
- Yu, C.-H., Peng, R.L., Luzin, V., Sprengel, M., Calmunger, M., Lundgren, J.-E., Brodin, H., Kromm, A., Moverare, J., 2020. Thin-wall effects and anisotropic deformation mechanisms of an additively manufactured Ni-based superalloy. *Addit. Manuf.* 101672.
- Yu, J., Rombouts, M., Maes, G., 2013. Cracking behavior and mechanical properties of austenitic stainless steel parts produced by laser metal deposition. *Mater. Des.* 45, 228–235.
- Zhang, H., Li, C., Dai, W., Liu, Y., Tian, S., Huang, W., Jia, D., He, D., Zhang, Y., 2020. Static compression testing CFRP single-lap composited joints using X-ray µCT. *Compos. Struct.* 234, 111667.
- Zhang, M., Sun, C.N., Zhang, X., Wei, J., Hardacre, D., Li, H., 2019. High cycle fatigue and ratcheting interaction of laser powder bed fusion stainless steel 316L: fracture behaviour and stress-based modelling. *Int. J. Fatigue* 121, 252–264.
- Zhu, C., Harrington, T., Gray, G.T., Vecchio, K.S., 2018. Dislocation-type evolution in quasi-statically compressed polycrystalline nickel. *Acta Mater.* 155, 104–116.
- Zhu, C., Livescu, V., Harrington, T., Dippo, O., Gray, G.T., Vecchio, K.S., 2017. Investigation of the shear response and geometrically necessary dislocation densities in shear localization in high-purity titanium. *Int. J. Plast* 92, 148–163.